ARCHIVE OF MECHANICAL ENGINEERING

DOI: 10.24425/ame.2024.151335 Early Access; pp. 1–21

Miroslaw RODZEWICZ [1]

Load spectra of a light unmanned aircraft – data recording frequencies and resulting measurement variations

Received 14 August 2024, **Revised** 30 September 2024, **Accepted** 8 October 2024, **Published online** 20 October 2024

Keywords: load spectra, unmanned aircraft, signal frequency, fatigue life

The article focuses on the load spectrum of a lightweight unmanned aircraft. It examines the impact of load signal sampling frequency on the load spectrum derived from the load signal. The flight sessions followed two scenarios: a maneuvering flight causing a wide range of load factor variations and a calm photogrammetric flight. The recorded load signals from two types of sensors were initially rescaled into load factor time series, with an optional signal smoothing process. These series were then downsampled by selecting every nth term, resulting in load factor sequences recorded at a lower frequency. Next, all sequences were transformed into sequences of local extremes of the Load Levels, resulting from quantifying the operational load variability into 32 intervals. Two options were considered: without filtering or with filtering of sequential pairs of terms generating small Load Level increments. Subsequently, the Rainflow Counting algorithm was applied, producing 32×32 load half-cycle arrays. Based on these arrays, incremental load spectra were calculated. The study provides a detailed comparison of load spectra for different load signal sources and recording frequencies. Additionally, calculations of the fatigue life of a structural element subjected to various load spectra were performed, leading to the formulated conclusions.

Nomenclature

a_z	an acceleration signal along the z-axis measured at the center of mass of the unmanned aircraft
D	a fatigue damage (see Palmgren-Miner formula)
FC-array	a full-cycle array
HC-array	a half-cycle array

✉ Miroslaw RODZEWICZ, e-mail: miroslaw.rodzewicz@pw.edu.pl
[1]Warsaw University of Technology, Warsaw, Poland

ILS	an incremental load spectrum
IMU_az	an acceleration signal has been recorded in the autopilot log
LL	Load Level – a standardized value of the load acting on the aircraft wings, expressed as integers, by dividing the total variability range into 32 intervals
LE_LL	Local Extremes chain of the Load Level time-series
LE_nz	Local Extremes chain of the load factor time-series
LS	a load spectrum
n_z	load factor
P-M	Palmgren-Miner hypothesis or formula
PSE	a principal structural element
REJ_az	a raw acceleration signal recorded by a supplementary measurement system
RE_ts	a raw wings-deflection signal recorded by a supplementary measurement system
REJ_tsw	smoothed signal $\mathrm{REJ}_{\mathrm{ts}}$
SLI-FILT	a filter of small load increments; (in the ILS charts, the signal descriptions use the designations "_0" or "_1" to indicate whether SLI-FIT was applied in signal processing)
ΔLL	the load level increment

1. Introduction

The increasing use of unmanned aviation in various civilian and military sectors [1–5], along with the growing density of UAV traffic in shared airspace, has underscored the importance of air operation safety [6, 7]. Safety is multifaceted, encompassing various aspects: starting from the human factor related to the drone operator's work [8], potential threats from interference in radio communication bands used in UAV operations [9], safety concerns related to the wear and tear of UAV propulsion systems [10], and the reliability of servomechanisms [11]. A critical safety factor is reliability, particularly the strength and fatigue life of the primary load-bearing structure of a UAV [12–14]. To demonstrate the fatigue durability of an aircraft's structure, it is essential to understand the load spectra acting on the aircraft. These spectra depend on its dynamic characteristics, air turbulence, control methods, and the specific mission being performed [15, 16]. The basis for determining the load spectrum is a thorough understanding of the time courses of loads on the key elements of the aircraft structure.

In the case of General Aviation aircraft, a load spectrum database was created in the 1970s [17]. This database is the result of extensive NASA research conducted for eight operational categories: (1) twin-engine executive, (2) single-engine executive, (3) personal, (4) instructional, (5) commercial survey, (6) aerial application, (7) commuter, and (8) aerobatic. The collected data enabled the statistical development of load spectra for gusts, maneuvers, and landings, as well as many other data concerning the distribution of load factor values and operational speeds and altitudes. This included examining the probability distributions of exceeding normal load factor values for a given flight condition. This database was systematically expanded by NASA until the late 1980s [15]. The data collected during the implementation of this program is still used today for fatigue calculations, both with

the classic Palmgren-Miner damage accumulation model and the methods based on fracture mechanics and damage tolerance [18].

Similar to manned aircraft, the loads on the primary load-bearing structure of unmanned aerial vehicles can be determined either by directly measuring structural deformations (which is the preferred method) or by analyzing time series of accelerations along the main structural axes recorded in the autopilot logs. This study investigates how the frequency of measuring and recording load data in the autopilot's digital memory impacts the resulting load spectrum and, consequently, the calculated fatigue life. Another area of interest is the effect of signal filtering on the obtained load spectrum. Specifically, the raw acceleration signal acting on the aircraft is affected by measurement noise, which can influence the results. Furthermore, the frequency spectrum of the acceleration signal is generally more complex than the frequency spectrum of the aircraft's structural response to applied accelerations. In this case, it pertains to deflection of wings which react to accelerations like an inertial component. This characteristic is due to the inertia of the wing structure, its stiffness, and damping coefficients, which depend on the construction material. These factors act as a natural low-pass filter, causing the wing deflections to lag behind rapidly changing accelerations beyond a certain frequency.

2. Experiments preparation

The research was conducted using the Sky Surfer, a small unmanned aircraft built from a commercially available kit. The aircraft's structure is made of expanded polypropylene (EPP) foam, reinforced with carbon rods (CFRP) that serve as the primary load-bearing framework. Fig. 1 illustrates the parameters of this model.

An autopilot model MATEK F405-WMN has been installed in the aircraft. For communication with the autopilot, mission planning, and log reading and review, an open-source software Mission Planner v.3.9 was used. In addition to its primary functions of controlling and stabilizing the aircraft during flight and enabling automatic navigation, each autopilot system includes a data acquisition system that gathers information from various sensors, including accelerometers. This data can be essential for analyzing load spectra. To determine the load spectrum of the primary load-bearing structure, it is necessary to record the acceleration signal along the z-axis measured at the aircraft's center of gravity (a_z-acceleration) [16]. The recording of the a_z signal in the autopilot log is particularly significant for the research conducted in this study, as it can be treated as a reference signal. This recording results from a complex process of processing the raw signal sampled at up to 1kHz (depending on settings), which is passed through low-pass and band-pass filters, and then logged at approximately 50 Hz. This frequency is an order of magnitude higher than what was possible with popular autopilots used a decade ago, allowing for more detailed analysis and comparison of how the logging frequency affects the calculated load spectrum.

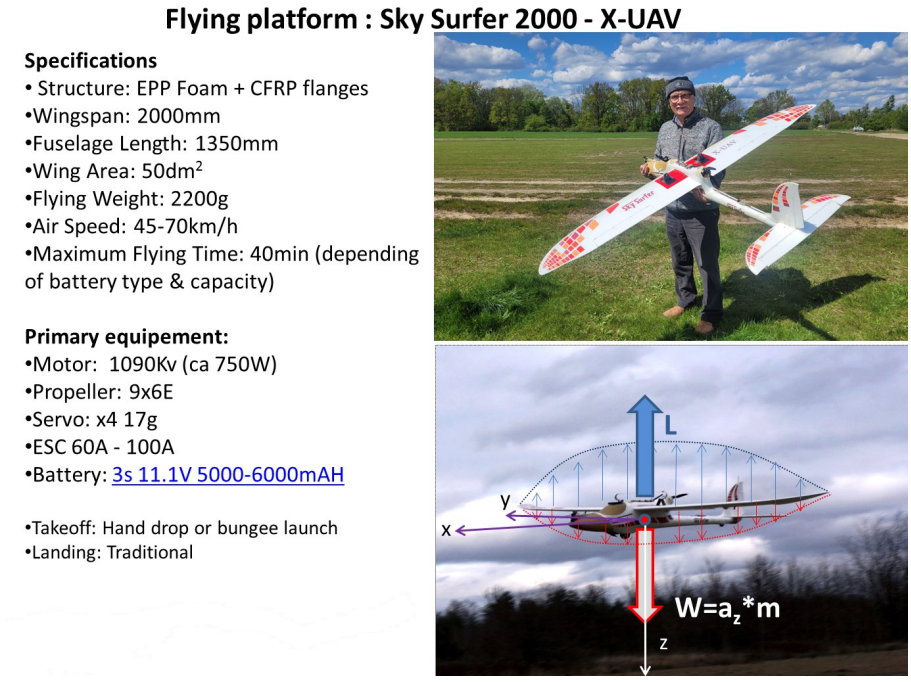

Fig. 1. Technical data of the flying platform used for experiments

Fig. 2 shows a fragment of the autopilot log, highlighting data related to an instantaneous value of acceleration a_z.

Additionally, the plane was equipped with a second, independent data acquisition system during measurement flights. This system used two sensors. The first was a 3-axis accelerometer with a range of $\pm 10g$, mounted very close to the aircraft's center of gravity, just above the autopilot, to ensure it experiences the same acceleration values as the autopilot sensor. The second sensor was a specially designed extensometer for measuring wing deflections, adhered to the upper surface of the wing (see Fig. 3). The measuring component in the extensometer was a bent spring made from a thin aluminum alloy sheet, with a strain gauge configured as a Wheatstone bridge attached. Wing deflection caused the spring to deform, resulting in a change in the signal from the strain gauge bridge. A miniature strain gauge amplifier powered by a 1s-LiPo battery was used to power the bridge and output the signal. The amplified signal from the strain gauge bridge was fed into one of the channels of a Logomatic v2 digital recorder. Signals from the 3-axis accelerometer, including the a_z signal, were fed into the other channels. Data was recorded at a frequency of 500 Hz per channel. No hardware signal filters were deliberately used in the independent data acquisition system. This was done to distinguish the load spectra derived from the raw signal and from the same signal after preliminary smoothing operations.

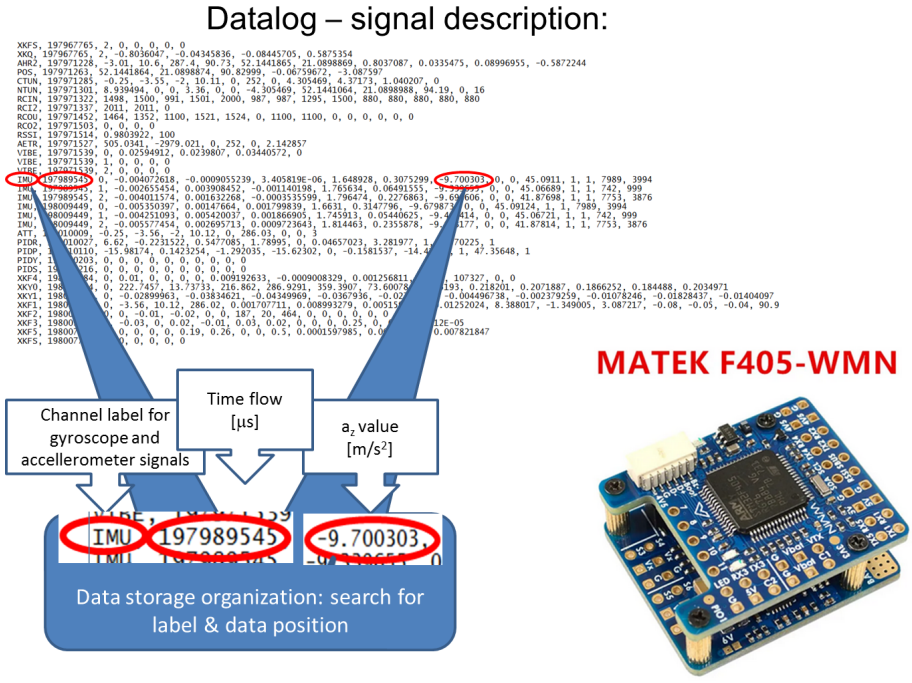

Fig. 2. The fragment of MATEK F-405 data-log; the text-line labeled IMU contains the records from gyroscopes and accelerometers

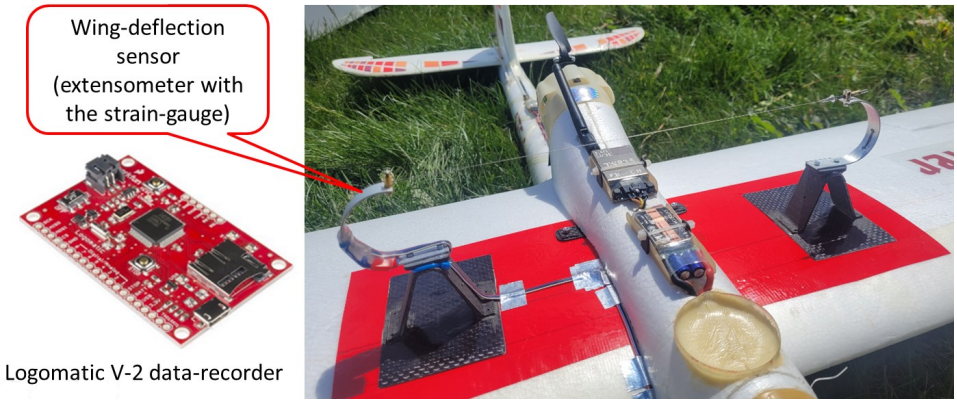

Fig. 3. Sensors of wings deflection

With two alternative sources of load signal (from an accelerometer and from a wing deflection sensor) recorded at a frequency of 500 Hz, it was possible not only to demonstrate the differences in load spectra derived from these alternative sources but also to compare the differences in load spectra obtained from signals recorded at different frequencies. By selecting every n^{th} value from the sequence recorded at 500 Hz, sequences corresponding to lower recording frequencies could be created. In this study, the following frequencies were chosen for the analysis: 50 Hz (matching the load signal recorded in the MATEK F-405 autopilot log) and 5 Hz (as seen in the logs of earlier generation autopilots).

3. Data acquisition – flight scenarios

To acquire measurement data, two flight sessions were organized based on different scenarios to obtain vastly differing load spectra. The first session's program included a test flight of the aircraft equipped with measurement systems to examine the dynamic characteristics of the loaded aircraft, adjust and trim the controls, and fine-tune the autopilot settings (particularly the PID parameters in the various control channels). During these tests, the functionality of the onboard measurement systems was also verified. Following this, the actual measurement flight was conducted, aiming to achieve the widest possible range of load factor variations within the maximum allowable loads. The scenario included maneuvers such as straight-flight "humps", tight spirals to the left and right, and turns. These maneuvers were performed manually using a controlled technique known as "brutal control". This flight will be referred to as the "maneuvering flight" in the subsequent parts of the article.

The scenario of the second flight session involved following a pre-programmed photogrammetric route while maintaining a constant speed and altitude, with bank angles in turns limited to 30°. Except for the landing phase, the entire flight was conducted in the automatic mode. The maneuvering flight lasted 7 minutes and 25 seconds, while the photogrammetric flight took 12 minutes and 29 seconds (with the photogrammetric task itself lasting 8 minutes and 40 seconds). For both sessions, takeoffs were assisted using a bungee cord. Both flights were conducted at the same airfield with light winds (approximately 4 m/s) from a similar direction. However, while non-thermal conditions were deliberately chosen for the maneuvering flight to avoid additional turbulence-induced loads, active thermal conditions were selected for the photogrammetric flight. This required increased autopilot activity to stabilize the aircraft, thereby enriching the spectrum of loads recorded. Autopilot logs from both flights, along with alternative load signal recordings, were used for further analysis in this study.

Below are charts with the main flight parameters and maps with recorded GPS traces, providing an overview of the measurement flights (see Figs. 4 and 5).

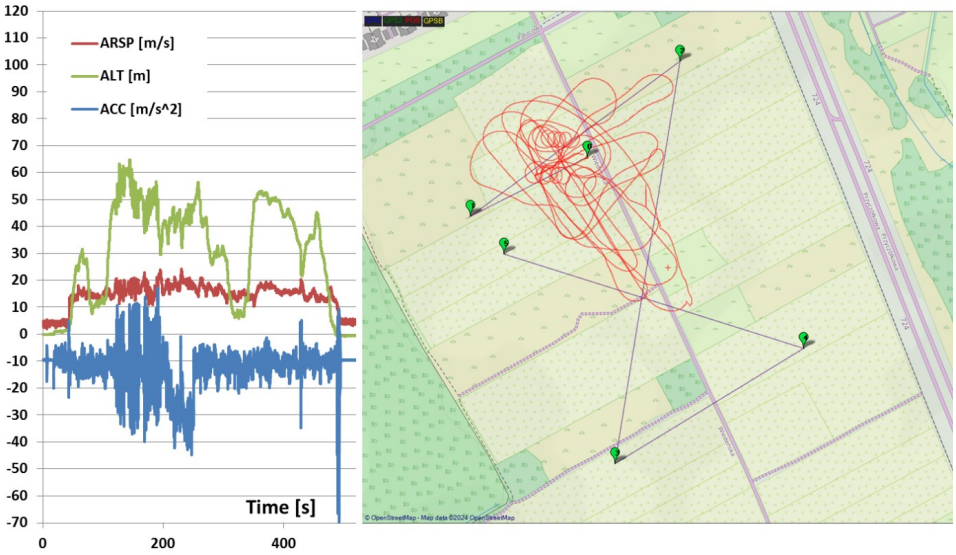

Fig. 4. Chart of key flight parameters and map with recorded GPS traces – maneuvering flight (log2024-01-05)

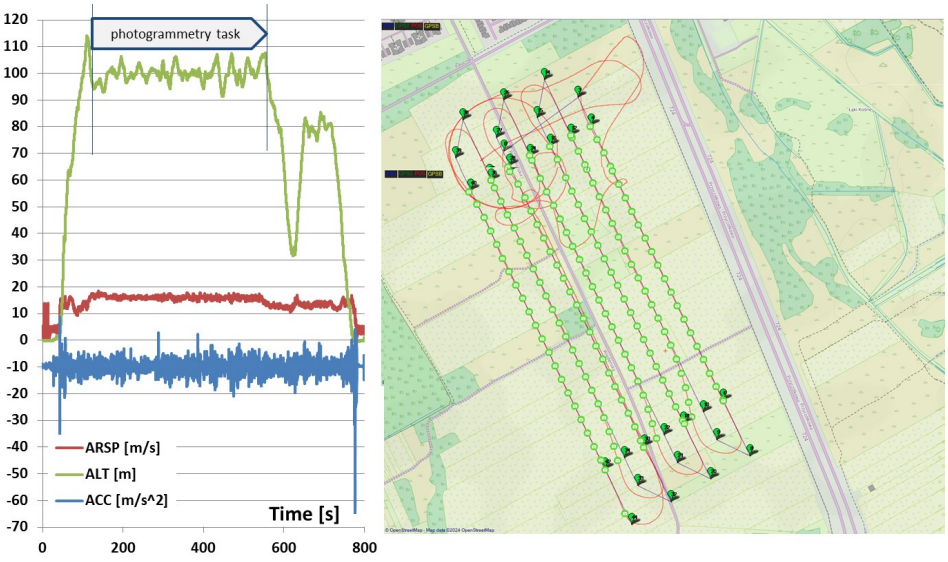

Fig. 5. Chart of key flight parameters and map with recorded GPS traces – photogrammetry flight (log2024-04-26)

4. Load signal processing procedure

In this study, to determine the load spectrum, a standard procedure for signal processing of aircraft structural loads was used, based on the Rainflow Counting algorithm and load half-cycle arrays [19, 20]. However, certain processes were modified to suit the research objectives described here. The procedure was conducted in several steps according to the following scheme. The first step involved converting the sequence of values from the acceleration sensors and the sequence of values from the wing deflection sensor into sequences of load factor values, denoted as n_z. By definition, $n_z = a_z/g$, where g represents the acceleration due to gravity.

The second step involved converting the sequence of real numbers, formed by the n_z values recorded at the specified sampling frequency, into a sequence of integers ranging from 1 to 32, representing the so-called Load Levels (LL). The conversion from n_z to LL was performed according to the standard formula established by the pioneers of tabular presentation of load spectra [21]:

$$n_{z\,\max} \Longrightarrow \mathrm{LL} = 3 \qquad \text{and} \qquad n_{z\,\min} \Longrightarrow \mathrm{LL} = 31\,. \tag{1}$$

The permissible operational load range of the aircraft is within the interval $3 \leqslant \mathrm{LL} \leqslant 31$. The load levels LL = 1, 2 and 32 are reserved for recording incidental, minor exceedances beyond the allowable operational range (which are undesirable but may occur against the intent of the aircraft operators).

The third step involves filtering the sequence of LL values into a sequence of local extremes of LL (abbreviated as LE_LL). In this sequence, for any chosen 3 consecutive elements, if the transition from one value to the next involves an increase in LL, then the transition between the 2nd and 3rd values must involve a decrease in LL (and vice versa). Concurrently with the LE_LL sequence, a corresponding sequence of LE_nz values is created for the next step by selecting them from the original n_z sequence established in the first step.

The fourth step (optional) is filtering the sequence of local extremes LE_LL by eliminating pairs of sequential elements that generate increases smaller than the width of one LL interval (i.e., eliminating load signal transitions where $\Delta\mathrm{LL} < 1$). The rationale is that increases smaller than $\Delta\mathrm{LL} = 1$ can randomly affect the load spectrum, as they depend on the momentary drift of the signal. If the signals were slightly shifted, some sequential pairs of local extremes would fall within the same LL interval, resulting in no transition between adjacent LL intervals, thus automatically excluding such increases from the record.

To perform this operation, the LE_nz sequence created in the previous step is used to check the actual increase values in the LE_LL sequence. The threshold value Δn_z for this operation can be adjusted. The LE_LL filtering option was created to numerically assess the impact of very small load signal increases on the load spectrum and the calculated fatigue life. This filtering is referred to in

the text as the SLI-FILT operation (small load increments filter). This operation is illustrated in Fig. 6.

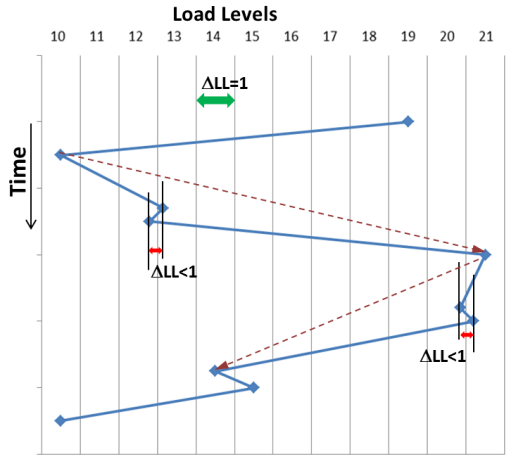

Fig. 6. Concept of the SLI-FILT operation, which involves eliminating local extremes with increments of ΔLL<1

The fifth step involves applying the Rainflow Counting algorithm to analyze the LE_LL sequence and generate the HC-array, a 32×32 matrix of half-cycle loads. This array is a specific form of the transfer array [22], where the transitions of the LE_LL signal are recorded according to the "from the LL to the LL" principle. Here, "from the LL" corresponds to the row number and "to the LL" corresponds to the column number, as illustrated in Fig. 7.

In both arrays, the main diagonal connecting the cells indexed at 1,1 and 32,32 is referred to as the “zero diagonal” (see Fig. 7). The HC-array differentiates itself from a standard transfer array by incorporating the Rainflow counting algorithm, which records cumulative signal increments of LE_LL (resulting from a sequence of multiple consecutive changes in the LE_LL signal). A common feature of both arrays (besides having the same graphical layout) is that the sum of all signal transfers recorded in the cells of the transfer array and the HC-array is identical and equals the number of local extremes in the LE_LL sequence minus 1. Additionally, the active area of both arrays (i.e., the rectangular envelope encompassing all rows and columns containing at least one non-zero value) is the same. This property is used as one of the checks for the correctness of the calculations performed. To simplify fatigue calculations, the HC-array can be transformed into a full cycle load array (FC-array), where the number of load cycles is recorded only on one side of the “zero diagonal”. This is possible because one full load cycle consists of two half-cycles (one associated with load increase and the other with load decrease). If one of these half-cycles is marked in the HC-array cell indexed at i,j, the other half-cycle is marked in the cell indexed at j,i.

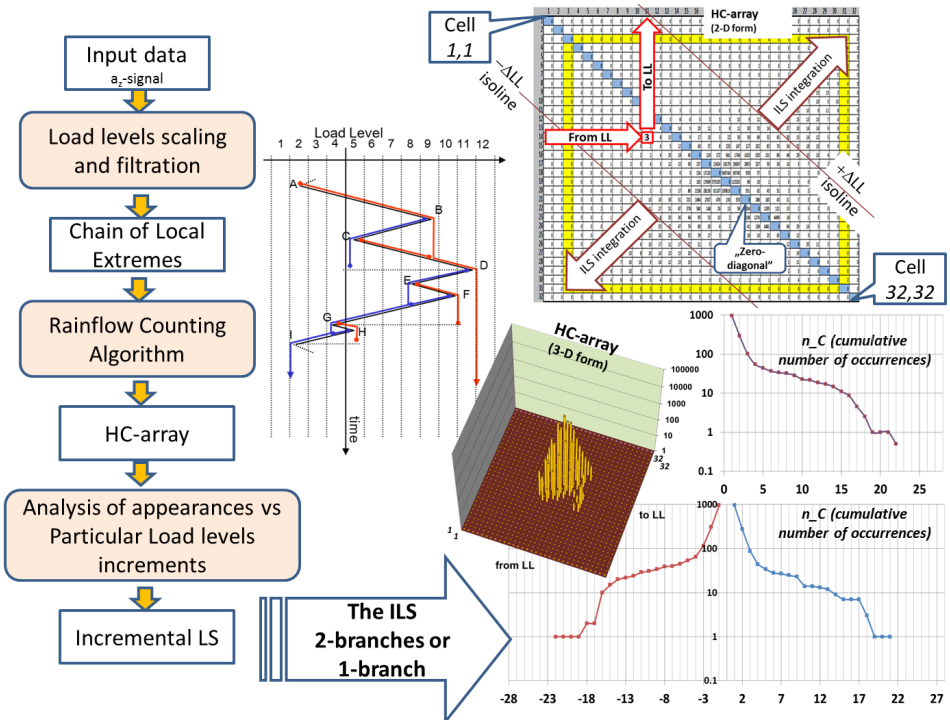

Fig. 7. Standard procedure of the load spectra derivation algorithm

The sixth step is to create Incremental Load Spectra (ILS), which are very useful for comparing load spectra from different flights or various signal sources.

5. Description of the conducted analyses

Due to the fact that the signal from the extensometer measuring wing deflection can only be correlated with the acceleration signal during free flight phases [22] (without the aircraft being in contact with the ground or a bungee cord), the comparative analysis of load signals from both sources is limited to the fragments of the flight from the moment the aircraft takes off until just before the landing gear touches the ground. In this study, the beginning of the analyzed time series of load signals was additionally delayed by approximately 15 seconds from the moment of takeoff, due to the rheological specifics of the tested system (the wings made of elastic polymer foam, mounted on a flexible CFRP tube, form a mechanical system where deformations are slightly delayed relative to the variable force (excitation) depending on the frequency of these force changes. The current value of the wing deformation is significantly influenced by both quasi-viscous damping of the wing's bending movements and dry friction between the spar tube and the sheath within the foam structure of the wing). This caused that a stabilization period was necessary

after the change in the force system acting on the wing post-takeoff to achieve a stable correlation between the signals from the accelerometer and the extensometer. Fig. 8 illustrates how these signals are correlated. Although this correlation is not as strong as in similar studies conducted on a professional composite glider structure [22], it was deemed sufficient for the analyses conducted in this study.

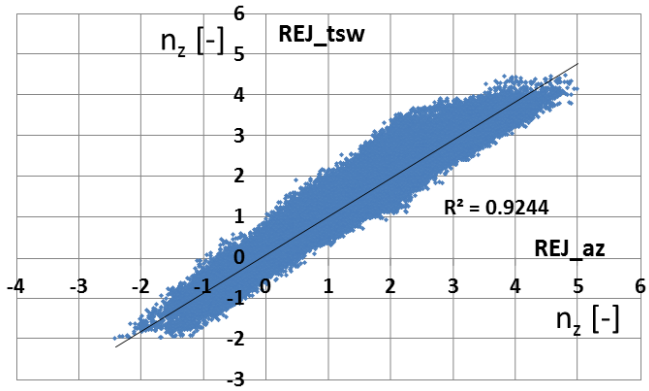

Fig. 8. Indication of extensometer signal vs indication of accelerometer signal – both scaled in n_z values

The load signals from various sources, scaled in n_z units, are designated as follows:

- IMU_az: signal from the autopilot accelerometer MATEK F405-WMN.
- REJ_az: raw signal from the accelerometer connected to the Logomatic v2 recorder.
- REJ_ts: raw signal from the extensometer connected to the Logomatic v2 recorder.
- REJ_tsw: smoothed signal from the extensometer.

The smoothing of the extensometer signal involved applying a moving average that included the currently considered series term plus the three terms following it, as well as a moving average that included the currently considered series term plus the three terms preceding it. This method avoided phase shift in the smoothed signal and assigned double weight to the current series term compared to the three terms before and after it. The result of this operation was a noticeable smoothing of the time series without significantly compromising the amplitude of the signal's peak values.

The main topics of the analysis are as follows:

- Investigating the impact of recording frequency of time series load signals from various sources on the load spectrum and calculated fatigue life.
- Examining the effect of the SLI-FILT operation (i.e., eliminating local extremes in the load signal series from pairs of series terms that result in small increments ΔLL). This study presents calculation results for a threshold of 0

(no elimination) and a threshold corresponding to 0.99 of one interval value ΔLL. Assuming the aircraft under study has $n_{z\,\max} = 5$ and $n_{z\,\min} = -3$, and using formula (1), we obtain the width of one LL interval as 0.2857. Therefore, a threshold of 0.99 means that pairs of local extreme terms resulting in increments lower than 0.282857 were eliminated. For clarity in incremental load spectrum graphs, these threshold values are denoted as _0 or _1 on ILS graphs.

- Comparing the differences between a mild load spectrum (acquired during photogrammetric flights in automatic mode) and a developed load spectrum (acquired during maneuvering flights with manual control), and assessing their effects on the calculated fatigue life.

6. Presentation of analysis results

The following flight time segments were analyzed: for the maneuvering flight: 430 seconds, and for the photogrammetric flight: 716 seconds. Fig. 9 presents the time courses of the load signal from the maneuvering flight for different recording frequencies. Since the load signal graphs from various sources are similar, only

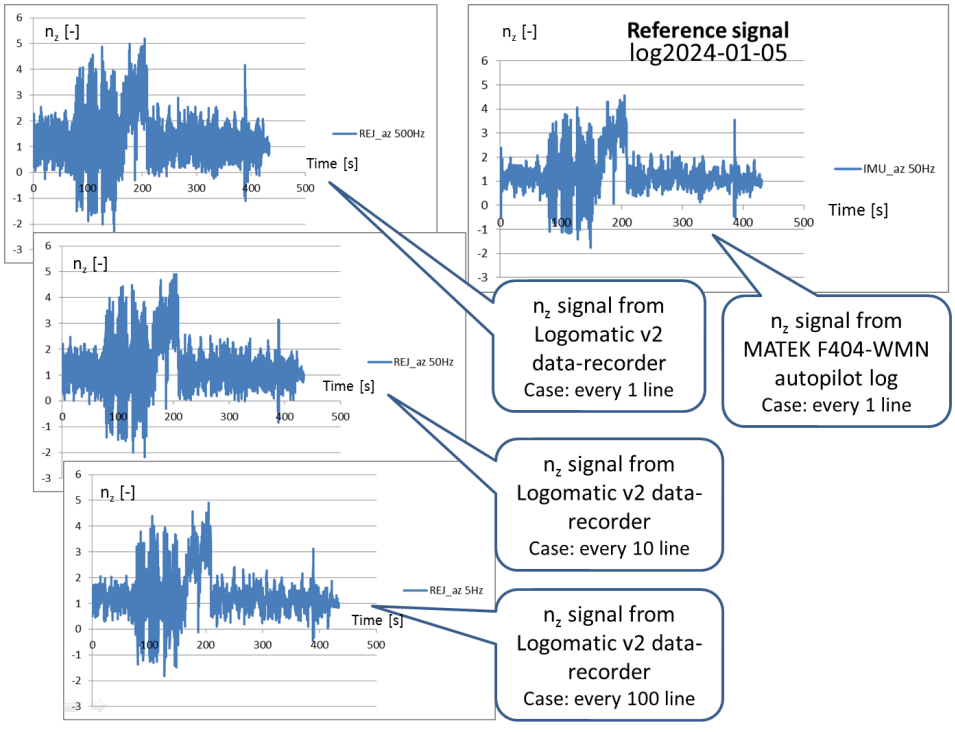

Fig. 9. Maneuvering flight – comparison of REJ_az load signal time courses for recording frequencies of 500 Hz, 50 Hz, and 5 Hz

the raw REJ_az signal and, for comparison, the IMU_az signal are shown in the presented graphs. It is evident that reducing the recording frequency does not significantly affect the shape of the time courses. It is also noticeable that in the filtered and noise-free IMU_az signal, the peak nz values are slightly lower compared to the REJ_az signal.

Although the time series plots of the load signals in Fig. 9 are similar, the sequences of local extrema for the considered frequencies, after undergoing the Rainflow Counting procedure, reveal distinct differences in the incremental load spectra. These differences can be observed in Figs. 10 and 11, which compare the incremental load spectra for the same signals.

Note: To enhance the clarity of the drawings and assist the reader in distinguishing subtle differences between the lines representing solutions for various input data options, 1-branch ILS charts are utilized in the article.

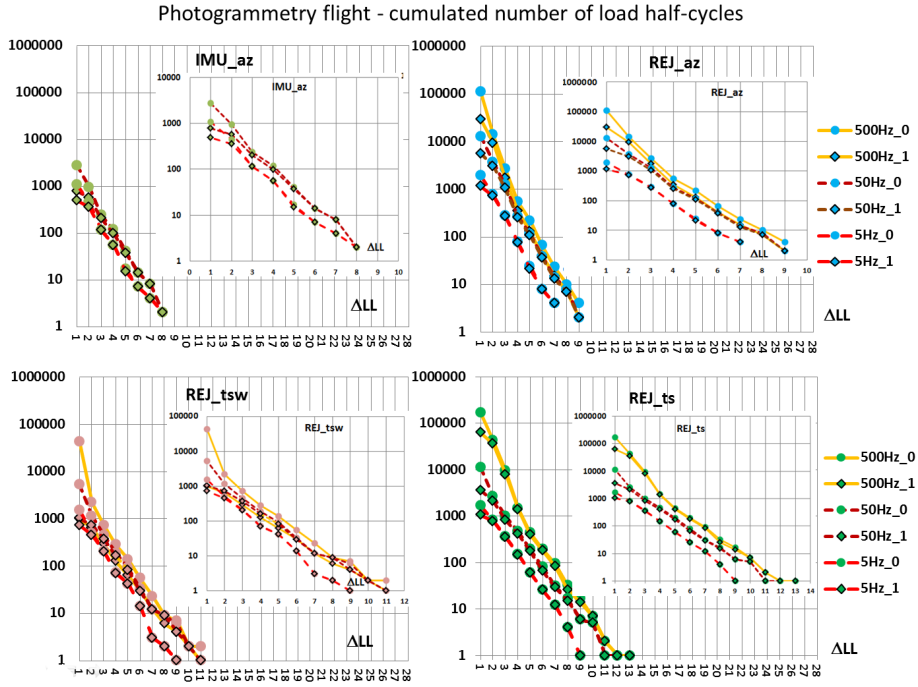

Fig. 10. Comparison of the ILSs derived from various sources of the load signal recorded during the photogrammetry flight (right: filtered signals; left: unfiltered signals)

The effects of the SLI-FILT operation can be observed in Fig. 12. Typically, these effects involve a reduction in the number of load half-cycles for the values of $\Delta LL = 1$, which aligns with expectations. They may also manifest as a reduction in the range of LL variability by one interval, as seen in the example of the IMU_az signal. Overall, in the case of photogrammetric flights, this effect is blurred due to the higher noise content in the analyzed signals.

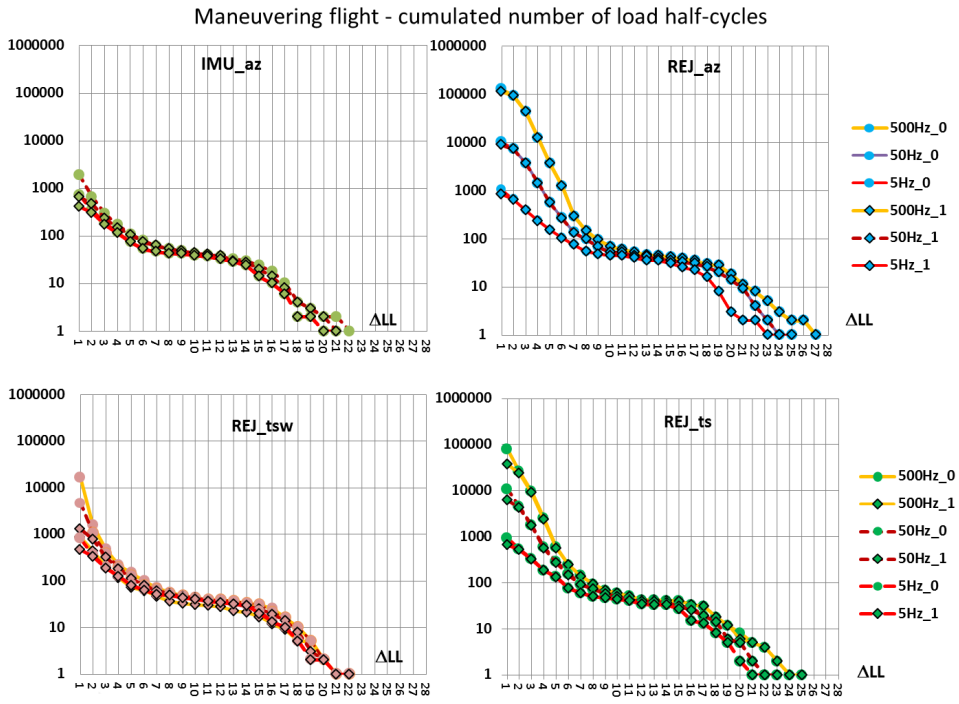

Fig. 11. Comparison of the ILSs derived from different sources of the load signal recorded during maneuvering flight (right: filtered signals, left: unfiltered signals)

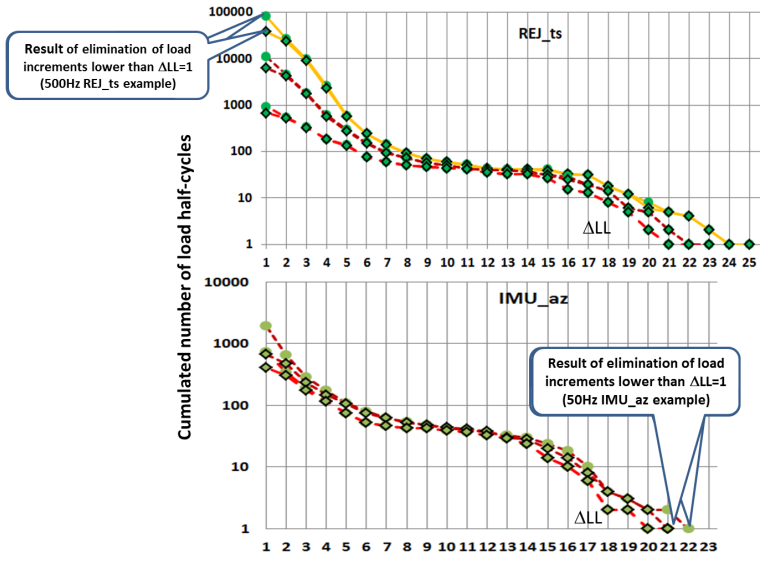

Fig. 12. Demonstration of the effect of the SLI-FILT operation

The analysis of the presented graphs leads to the following conclusions:

1. Regardless of the signal source, the computed load spectrum from the photogrammetric flight is significantly milder than the load spectrum from the maneuvering flight. On the vertical axes of the ILS graphs for both analyzed flights, the ranges of variability in the cumulative number of load half-cycles are similar for the spectra based on the same signal sources. However, on the horizontal axes, the maximum load increments (ΔLL) are more than twice as low for the photogrammetric flight. Interestingly, the cumulative number of load half-cycles for ΔLL values close to 4 is similar across all ILSs obtained from filtered signals.

2. Since the range of changes and variations in the load factor during the photogrammetric flight are relatively small, the significant impact of measurement noise becomes apparent, causing scatter in the lines representing ILS for different signal recording frequencies. This scatter is reduced in the case of filtered signals, with the smallest scatter observed for the ILS obtained from the IMU_az signal, which, as previously mentioned, is the best-filtered and noise-free signal in this set.

3. The load spectra from the maneuvering flight differ depending on the signal source. For filtered signals (IMU_az and REJ_tsw), these differences are relatively small across the entire range of ΔLL, regardless of the signal recording frequency. However, for noisy signals (REJ_az and REJ_ts), the recording frequency significantly impacts the number of half-cycles, especially for $\Delta LL < 8$ and $\Delta LL > 15$. This suggests that the measurement noise in REJ_az and REJ_ts signals is broadband and can include high-amplitude oscillations that occur briefly at high frequencies during sharp maneuvers. Consequently, the Rainflow Counting algorithm detects a higher number of half-cycles with large ΔLL values.

4. The SLI-FILT operation, which eliminates pairs of local extrema in the load signal that result in increments below a set threshold, has a noticeable effect primarily on smoothed signals (IMU_az and REJ_tsw). The graphs show that the ILS lines with diamond markers (i.e., results obtained using the SLI-FILT operation) are more clustered regardless of the recording frequency. The above conclusions pertain only to the graphical layout of the lines representing individual ILS on the graphs. From a practical perspective, the most interesting aspect is how the differences in load spectra will affect fatigue durability. This topic is addressed in the following chapter.

7. Calculations of fatigue life

To measure the impact of differences between various ILSs, as shown in Figs. 10 and 11, fatigue calculations were conducted. These calculations were based on the classical Palmgren-Miner (P-M) hypothesis, whose application to the fatigue life calculations of light aircraft structures is detailed in Report AFS-120-73-2 [23].

It was assumed that the test element, representing the so-called Principal Structural Element (PSE) made of aluminum alloy, would be subjected to the aforementioned load spectra. The fatigue properties of this alloy were provided

in the Report as a set of S-N curves, which show the number of cycles to failure depending on the amplitude of variable stress cycles and the mean value of variable stress cycles. Therefore, the calculated fatigue life results refer not to the structure of the aircraft described in the study, but to this test element, which is used to assess the effect of different load spectra. Compared to the calculation method presented in Report AFS-120-73-2, this study employed an updated calculation algorithm using 32×32 tables that record the material's fatigue properties, constructed similarly to the HC-array. Consequently, the classical P-M hypothesis formula was modified to the following form:

$$D = \chi \sum_{i=1}^{32} \sum_{j=1}^{32} D_{i,j} = \chi \sum_{i=1}^{32} \sum_{j=1}^{32} \frac{n_{i,j}}{N_{i,j}}. \tag{2}$$

Symbol χ is the coefficient equal to 1 or 0.5 depending on the kind of transfer arrays used for calculations (i.e., a FC-array or a HC-array).

In this model, $N_{i,j}$ represents a cell in the HC-array (or FC-array) containing the number of cycles (or half-cycles) to failure, while $n_{i,j}$ denotes the value identical to the content of the HC-array cell. When transforming S-N curves into an array of number of half-cycles to failure (N-array), it was assumed that the stresses in the PSE are proportional to the value of n_z. It was assumed that for $n_z = 1$, the stresses are 26 MPa, and based on this, auxiliary 32×32 tables containing information on the amplitude and mean stress value in the PSE were determined. Using these data and the linear form of the S-N curves presented in the Report on a logarithmic scale, the number of half-cycles to failure for each cell in the N-array was interpolated. This array is shown in Fig. 13. The yellow area represents interpolated values, while the orange area represents extrapolated values (i.e., those beyond the empirically verified range). For the accuracy of fatigue life calculations, it was crucial that all non-zero cells in the HC-array matched the cells in the N-array within the yellow area. Fatigue calculations were performed using Excel. The results are presented in Fig. 14.

The graphs indicate that the most significant differences in fatigue durability for various load signal recording frequencies occur with unfiltered signals REJ_az and REJ_ts. In the case of the photogrammetric flight (where the ratio of noise to the range of variability of the measured load signals was greater), the differences in results are much greater compared to the maneuvering flight. The application of the SLI_FILT operation affects the fatigue durability calculations. This impact is significantly greater for filtered signals IMU_az and REJ_tsw than for unfiltered signals REJ_az and REJ_ts. This suggests that measurement noise in the unfiltered signals exceeds the value of $\Delta LL = 1$.

Upon comparing the results of fatigue life calculations for load spectra derived from unfiltered maneuvering flight signals, it is evident that the fatigue life estimated using the REJ_ts signal surpasses that calculated using the REJ_az signal. This indicates that the load spectrum obtained from the REJ_ts signal is milder than the

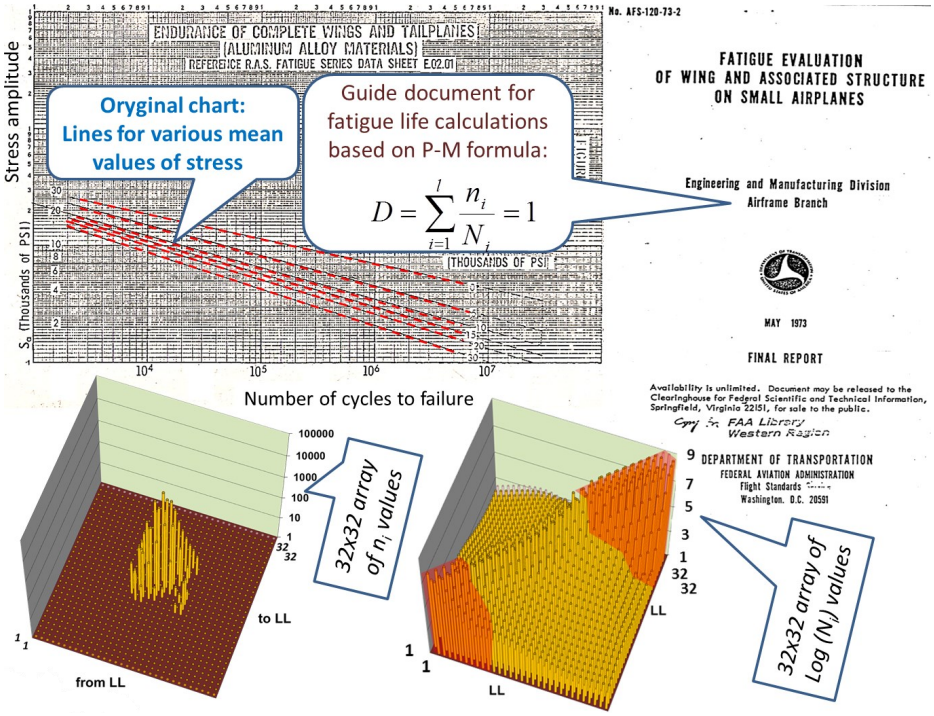

Fig. 13. Application of transfer arrays for fatigue life calculation

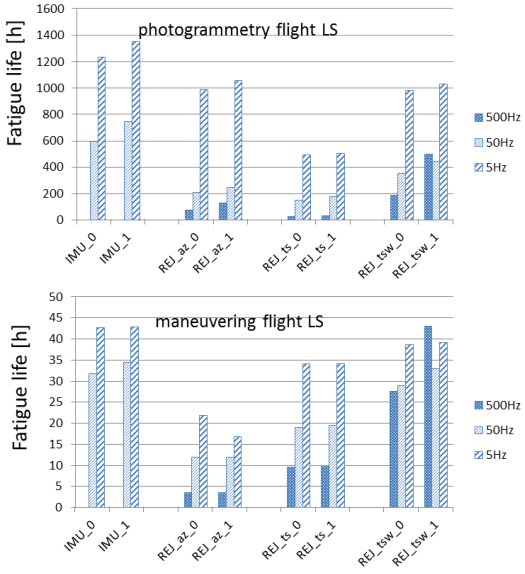

Fig. 14. Results of fatigue life calculations for load spectra based on the load signal source, recording frequency, and the threshold applied for filtering small ΔLL increments

spectrum obtained from the REJ_az signal. This fact supports the thesis that the inertia of the wing structural framework and its rheological characteristics act as a natural low-pass filter, smoothing the time course of the REJ_ts signal.

The fatigue life calculation results for the load spectra derived from the filtered IMU_az and REJ_tsw load signals from the maneuvering flight are very similar. Therefore, these signals can be used interchangeably, provided they do not include the takeoff and landing phases.

It is important to note that the results presented here pertain to PSE, whose fatigue properties are suitable for the aluminum alloy specified in the AST report. Such PSEs are often found in the construction of unmanned aerial vehicles. If the PSE were made from a composite material (e.g., CFRP), the results would differ, as FRP composites have different fatigue properties. These properties strongly depend on the fiber reinforcement layer arrangements, which must be rationally aligned with the loads acting on the structure. With the correct fiber arrangement, composite structures exhibit low fatigue sensitivity to load increments corresponding to $\Delta LL < 4$ [22]. Consequently, these small load increments can be omitted in the load spectrum created for fatigue testing. This is the most significant feature distinguishing them from metals. For the Sky Surfer 2000, a composite wing spar in the form of a unidirectional CFRP tube can be selected as the PSE. This spar is subjected to bending and shear forces. The study did not address this type of PSE due to the lack of data on the fatigue characteristics of the aforementioned composite under such loads.

8. Summary and final conclusions

The general conclusion from the calculations is that, regardless of the considered load signal, the fatigue life of the PSE for the photogrammetric flight load spectrum is 20 to 30 times greater than the fatigue life calculated for the maneuvering flight load spectrum.

In fatigue calculations, a crucial aspect is the conservatism of the results. A result is considered conservative when the calculated fatigue life is underestimated. Conversely, overestimating fatigue life poses a safety risk if operational regulations for an aircraft are based on such results. On the other hand, relying on underestimated fatigue life enhances safety but negatively impacts economic indicators, as the aircraft structure would require more frequent technical inspections and/or earlier replacement of critical components that limit the structure's fatigue life, depending on the adopted operational model.

The variability in fatigue life results calculated in this study, based on load signals recorded by sensors measuring acceleration or wing deflection, should be interpreted such that a higher result represents a less conservative outcome compared to a lower result.

Using unfiltered load signals for fatigue life calculations yields the most conservative results but is irrational for the following reasons:

1. these results are highly dependent on the signal sampling frequency;
2. at high recording frequencies, signal noise increases the contribution of small load increments in producing the value D in the P-M formula, causing the fatigue life calculation results to become excessively underestimated.

Reducing signal noise is a crucial issue. A high level of measurement noise in load signals recorded during a flight with minimal load factor variation undermines the validity of fatigue life assessments and the imposition of operational limits for a given aircraft. Results based on unfiltered signals should be considered only as an indication of the possible range of fluctuations in results generated by such signals.

Since it is not rational for the outcome of fatigue life calculations to depend on the load signal sampling frequency, special attention should be given to selecting appropriate signal filters (e.g., Kalman filter) and optimizing their parameters. The aim is to avoid excessive filtering, which smooths out load signals, thereby flattening the variability in fatigue life calculations for different load signal sampling frequencies but also making these load spectra less conservative. Therefore, more detailed studies are necessary to distinguish between real load changes and mere measurement noise in the recorded load signal.

The data set should be expanded (by conducting multiple measurement flights) to enable statistical analysis of load spectra from these flights. The measurement flight scenarios should be standardized and include both repeatable phases of automatic flight and repeatable manual maneuvers designed to generate distinct load spectra, weaker than those observed in the maneuvering flight described in this study, but significantly stronger than those in the photogrammetric flight. Flight sessions should be conducted under varying atmospheric turbulence conditions. Such studies are planned for future work.

Acknowledgement

The author extends gratitude to those who contributed to the creation of this article: J. Hajduk for assistance and piloting the aircraft during measurement flights, and G. Czerwiński for developing the program for processing data from the autopilot logs.

References

[1] S.K. Chaturvedi, R. Sekhar, S. Banerjee, and H. Kamal. Comparative review study of military and civilian unmanned aerial vehicles (UAVs). *INCAS Bulletin*, 11(3):181–182, 2019. doi: 10.13111/2066-8201.2019.11.3.16

[2] P. Radoglou-Grammatikis, P. Sarigiannidis, T. Lagkas, and I. Moscholios. A compilation of UAV applications for precision agriculture. *Computer Networks*, 172:107148, 2020. doi: 10.1016/j.comnet.2020.107148.

[3] S.A.H. Mohsan, N.Q.H. Othman, Li Y, M.H. Alsharif, and M.A. Khan. Unmanned aerial vehicles (UAVs): practical aspects, applications, open challenges, security issues, and future trends. *Intelligent Service Robotics*. 16(1):109–137, 2023. doi: 10.1007/s11370-022-00452-4.

[4] K. AL-Dosari,Z. Hunaiti, and W. Balachandran. Systematic review on civilian drones in safety and security applications.*Drones* 7(3): 210, 2023. doi: 10.3390/drones7030210.

[5] T. Goetzendorf-Grabowski, A. Tarnowski, M. Figat, J. Mieloszyk, and B. Hernik. Lightweight unmanned aerial vehicle for emergency medical service – Synthesis of the layout. *Proceedings of the Institution of Mechanical Engineers, Part G: Journal of Aerospace Engineering*, 235(1):5–21, 2021. doi: 10.1177/0954410020910584.

[6] W. Stecz and P. Kowaleczko. Designing operational safety procedures for UAV according to NATO architecture framework. In *Proceedings of the 16th International Conference on Software and Data Technologies*, pages 135–142, 2021.

[7] W. Wang, X. Guo, Y. Liu, A. Tang, and Q. Yang. Factors affecting unmanned aerial vehicles' unsafe behaviors and influence mechanism based on social network theory. *Transportation Research Record*, 2677(5):1030–1045, 2023. doi: 10.1177/03611981221138782.

[8] E.S. Jahanpour, B. Berberian, J.P. Imbert, and R.N. Roy. Cognitive fatigue assessment in operational settings: a review and UAS implications. *IFAC-PapersOnLine*, 53(5):330–337, 2020. doi: 10.1016/j.ifacol.2021.04.188.

[9] M. Krichen and A. Mihoub. Unmanned aerial vehicles communications security challenges: a survey. In: M. Abdelkader, A. Koubaa (eds) *Unmanned Aerial Vehicles Applications: Challenges and Trends*. Springer, Cham. 2023. doi: 10.1007/978-3-031-32037-8_12.

[10] M. Noor, Z. Fang, and Y. Cao. Fatigue life estimation of fixed-wing unmanned aerial vehicle engine by grey forecasting. *Measurement and Control*, 54(5-6):799–810, 2021. doi: 10.1177/0020294020915215.

[11] A. ElSaid, D. Adjekum, J. Nordlie, and F.A. El Jamiy. A test-bed for measuring UAS servo reliability. *Aerospace*, 6(9):96, 2019. doi: 10.3390/aerospace6090096.

[12] A. Kurnyta, W. Zielinski, P. Reymer, K. Dragan, and M. Dziendzikowski Numerical and experimental UAV structure investigation by pre-flight load test. *Sensors*, 20(11):3014, 2020. doi: 10.3390/s20113014.

[13] S.N. Satish Kumar, T.L. Rakesh Babu, and M. Ramesh. Fatigue and vibrational analysis of drone by using composite and mmc alloys for military applications. *International Research Journal of Engineering and Technology (IRJET)*, :7(7):5650–5665, 2020.

[14] G.D. Jin, L.B. Lu, L.X. Gu, J. Liang, and X.F. Zhu. Fatigue life of UAV airframe based on damage coefficient. *Advanced Materials Research*, 709:358–362, 2013. doi: 10.4028/www.scientific.net/AMR.709.358.

[15] J.E. Locke, H.W. Smith, E.A. Gabriel, and T. DeFlore. *General Aviation Aircraft-normal Acceleration Data Analysis and Collection Project*. Report No DOT/FAA/CT-91/20, University of Kansas Flight Research Laboratory, 1993.

[16] M. Rodzewicz, D. Głowacki , and J. Hajduk. Comparative analysis of the load spectra recorded during photogrammetric missions of lightweight UAVs in tailless and conventional configurations. *Fatigue of Aircraft Structures*, 2022(14):114-134, 2022. doi: 10.2478/fas-2022-0009.

[17] L.E. Clay, R.L. Dickey, M.S. Moran, K.W. Payauys, andT.P. Severyn. Statistical analysis of general aviation VG-VGH data. NASA Report No. NASA-CR-132531 prepared under Contract No. NAS1-12389 by Technology Incorporated Instruments and Control Division, Dayton, Ohio, 1974.

[18] H. Millwater, J. Ocampo, G. Singh, H. Smith, and E. Meyer. Probabilistic Structural Risk assessment and risk management for small airplanes. Report No. DOT/FAA/AR-11/14, sponsored by U.S. Department of Transportation, Federal Aviation Administration, Kansas City, 2017.

[19] M.S. Łukasiewicz. Load spectrum analysis with open source software - an application example. *Fatigue of Aircraft Structures*, 2021(13):17–30, 2021. doi: 10.2478/fas-2021-0003.

[20] S. Gajek. Automation of aircraft fatigue life estimation. *Fatigue of Aircraft Structures*, 2022(14):83–103, 2022. doi: 10.2478/fas-2022-0007.

[21] H. Kossira and W. Reinke. Entwicklung eines Belastungskollektivs fur leichte Motorflugzeuge aus den Beanspruchungsmessungen an einem Segelflugzeug (Development of a load spectrum for light aircraft based on stress measurements from a glider). IFL-IB 86-04, TU Braunschweig, 1986. (in German).

[22] M. Rodzewicz. Investigation of the Glider Load Spectra. *Technical Soaring*, 31(1):2–12, 2007.

[23] Engineering and Manufacturing Division, Airframe Branch. Fatigue evaluation of wing and associated structure on small airplanes. Report No. AFS-120-73-2, sponsored by Department of Transportation, Federal Aviation Administration, Washington, DC, 1973.